OPEN

Correspondence and
requests for materials
should be addressed to
M.S. (mwshao@suda.
edu.cn) or S.-T.L.
(apannale@suda.edu.
cn)

Smart Liquid SERS Substrates based on Fe₃O₄/Au Nanoparticles with Reversibly Tunable Enhancement Factor for Practical Quantitative Detection

Fei Hu[1], Haiyang Lin[1], Zhaoshun Zhang[1], Fan Liao[1], Mingwang Shao[1], Yeshayahu Lifshitz[1,2]
& Shuit-Tong Lee[1]

[1]Institute of Functional Nano & Soft Materials (FUNSOM), Jiangsu Key Laboratory for Carbon-based Functional Materials and Devices & Collaborative Innovation Center of Suzhou Nano Science and Technology, Soochow University, Suzhou 215123, P. R. China, [2]Materials Science and Engineering Department, Technion, Israel Institute of Technology, Haifa 32000, Israel.

There is a strong correlation between the surface enhanced Raman scattering (SERS) enhancement factor (EF), the excitation wavelength, and the feature properties (composition, size, geometry, and analytes). The prediction of the EF of specific substrates, crucial to the quantitative SERS detection, is however still very difficult. The present work presents smart liquid SERS substrates consisting of suspensions of Fe₃O₄/Au nanoparticles, which provide high spot-to-spot uniformity, reproducibility and good reversibility. The EF of these substrates can be reversibly tuned by applying an external magnetic field. The EF magnetic tuning is within 2 orders of magnitude per substrate in the range of 10^4–10^7. The ability to reversibly adjust the SERS EF enables to reduce EF variations caused by external effects such as substrate-to-substrate differences and long-term-storage degradation. This improves the quantitative detection of analytes and might be a significant step forward in employing SERS for practical applications.

Surface-enhanced Raman scattering (SERS) has developed into an important surface analysis tool[1–4] since its discovery in the mid-1970s[5], offering rich information about analytes at trace or even single-molecule levels[6–9]. It is commonly accepted that there is a strong correlation among: (1) the SERS enhancement factor (EF), (2) the excitation wavelength, and (3) the geometry of the SERS substrates and the analyte[10]. Excellent SERS substrates have been consequently reported including controlled shape nanoparticle (NP) colloids[11], rough metallic surfaces[12], and nanoantennas[13]. Significant research efforts focused on periodically patterned SERS substrates (e.g. grating structures[14], engineered NP cluster arrays[15], and metallo-dielectric structures[16]), which form photonic crystals. The photonic bandgap inhibits the transmission of the Raman scattered photons in the normal incidence direction. Constructive interference of backward reflected Raman scattered photons enhances the Raman signal[17]. In spite of the progress made it is still a remaining challenge to predict reliably the EF of SERS targets from the excitation wavelength, adsorbate type and geometry of SERS substrates.

Iron oxide colloids have been recently found to form magnetically induced self-assembled periodic structures. Applications included bio- and chemical sensors, color paints and inks, and reflective display units[18,19]. Moreover, the possibility of tuning the photonic bandgap and precisely control the photonic crystals made from iron oxide colloids by applying an external magnetic field was recently reported[20]. The spacing between the iron oxide particles constituting the photonic crystal was reversibly tuned affecting the structure and the resulting properties of the photonic crystal. Inspired by this work we decided to use these iron oxide particles for the fabrication of SERS substrates in which the EF can be accurately and reversibly tuned by an external magnetic field.

The present work utilizes a liquid suspension of Fe₃O₄/Au NPs as SERS substrates. The coupling of localized surface plasma resonance and the unique optical properties of the colloidal photonic crystals yielded substrates with high and controllable SERS activity and excellent spot-to-spot reproducibility. Changing the strength of the externally applied magnetic field modifies the inter-particle distance of the photonic crystal and the resulting
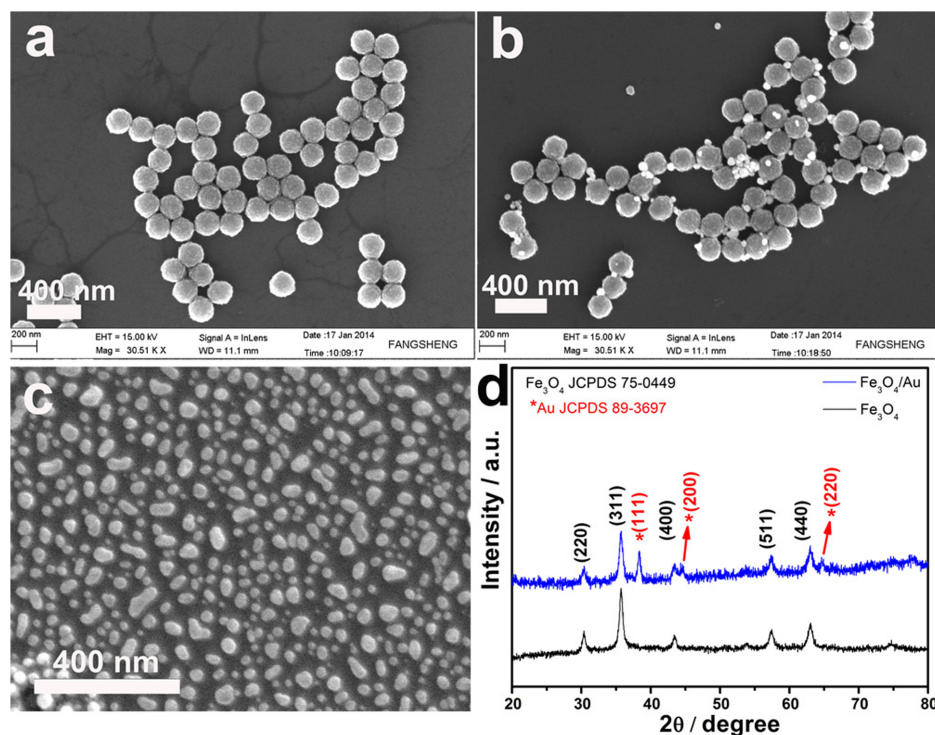
Figure 1 | SEM images of monodispersed NPs: (a) Fe₃O₄ NPs with average diameter of 180 ± 11 nm, (b) Fe₃O₄/Au NPs, (c) CTAB-capped Au NPs on silicon wafer; and (d) XRD patterns of prepared Fe₃O₄ NPs (black curve) and Fe₃O₄/Au NPs (blue curve) (volume ratio of Au : Fe₃O₄ = 40 : 1).

electromagnetic field distribution induced by the localized surface plasma resonance of the metallic NPs. Consequently, EF values of 10^4–10^7 are reversibly obtained in a controllable manner.

Results

Structure of Fe₃O₄, CTAB capped Au and Fe₃O₄/Au NPs. Fe₃O₄, CTAB capped/Au and Fe₃O₄/Au NPs were prepared as fully described in the Methods section. SEM showed that uniform, spherical Fe₃O₄ NPs with a diameter of 180 ± 11 nm were obtained (Figure 1a). The ζ potential of −33.8 mV of the Fe₃O₄ NPs indicates their high negatively charged surface. The as-prepared Au NPs were about 35 ± 7.2 nm (Figure 1c) in diameter and positively charged with a ζ potential of 12.6 mV as a result of their surface adsorption by the cationic surfactant (CTAB). Consequently, the negatively charged Fe₃O₄ NPs and the positively charged CTAB-capped Au NPs were electrostatically bonded (SEM imaging Figure 1b and TEM imaging Figure 2). The TEM images (Figures 2a–2c) show that each iron oxide NP attracts about 2 - 3 Au particles on its surface. Figure 2b is the high angle annular dark field scanning transmission electron microscopy (HAADF-STEM) image of a Fe₃O₄/Au NP. In the upper left corner of Figure 2b, the Au particles, which have a higher Z than the Fe₃O₄ particles (i.e. a more intense electron backscattering), are imaged as brighter dots[21]. Energy-dispersive X-ray spectrometry (EDS) mapping shows the elemental distribution of oxygen (red), iron (orange) and gold (blue), respectively (Figure 2b). The crystallinity of the as-prepared Fe₃O₄/Au NPs was confirmed by high-resolution TEM (HRTEM), (Figure 2d), which is the enlargement of the red square in Figure 2c. The lattice spacings of two adjacent planes of 0.30 and 0.48 nm correspond to the (220) and (1-11) planes of cubic magnetite. The 0.24 nm spacing of the face-centered cubic (FCC) Au crystallite corresponds to its (111) planes. X-ray diffraction (XRD) measurements further confirm the high degree of crystallinity of the Fe₃O₄/Au NPs (Figure 1d). All the diffraction peaks from the 20–80° scan can be indexed either to the (220), (311), (400), (511), and (440)

planes of the FCC Fe₃O₄ crystals (JCPDS Card No.75-0449); or to the (111), (200), (220) diffraction planes of the FCC Au crystals (JCPDS Card No.89-3697), respectively. The above characterizations show that a small quantity of CTAB-capped Au NPs decorated the surface
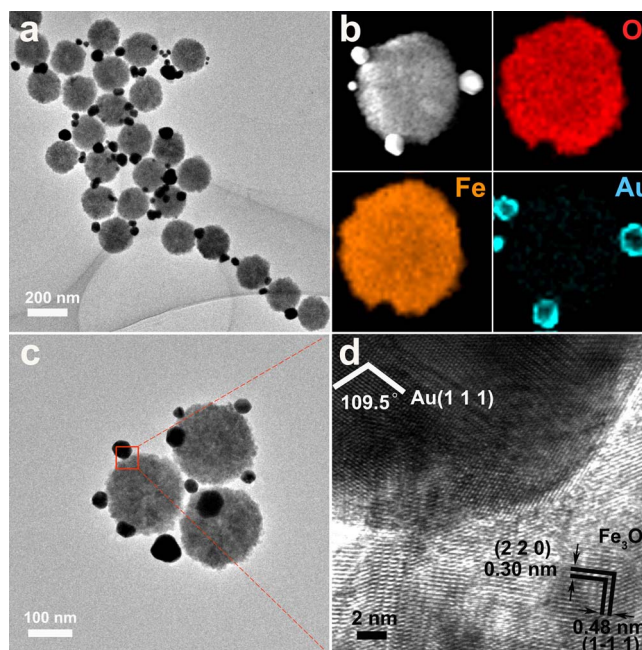
Figure 2 | (a) TEM image of Fe₃O₄/Au NPs; (b) HAADF-STEM image of a single Fe₃O₄/Au NP and EDS mapping revealed the elemental distributions of O (red), Fe (orange), and Au (bule); (c) TEM image showed that each monodisperse Fe₃O₄ NPs attracts about 2 ~ 3 Au NPs around the surface; and (d) HRTEM image taken from red square of (c) (volume ratio of Au : Fe₃O₄ = 40 : 1).

of each Fe_3O_4 NP (the Fe_3O_4 NPs serving as superparamagnetic building blocks) due to electrostatic incorporation.

**Optical absorption of the Fe_3O_4, CTAB capped Au and Fe_3O_4/Au NPs.** Figure 3a presents the UV-vis spectra of the pure Fe_3O_4, the capped CTAB Au, and as-prepared Fe_3O_4/Au NPs dispersions. The CTAB-capped Au NPs show a characteristic plasmon resonance band around 533 nm. Such a band is absent in the spectrum of the pure Fe_3O_4 NPs. The attachment of the capped Au NPs to the Fe_3O_4 NPs red-shifts the plasmon absorption peak by 27 nm with respect to that of the pure capped Au NPs. This red-shift is a result of the decoration of the Fe_3O_4 NPs by the capped Au particles.

The Fe_3O_4/Au NPs based magnetic field induced quasi-photonic crystal system. Figure 3b shows the photo images and reflection spectra of an aqueous solution of a Fe_3O_4/Au based quasi-photonic crystal system (ca. 5.2 mg mL^{-1}) in response to a varying magnetic field achieved by controlling the electric current of an electromagnet. The peak resulting from the diffraction of the photonic crystal based on the present Fe_3O_4 NPs of 180 nm in diameter blue-shifts from 699 to below 586 nm as the magnetic field increases from 9.5 to 22.2 mT. Note that the tuning range of the diffraction wavelength is related to the average size of the Fe_3O_4 NPs. The inter-particle distance in the z direction can be estimated by d in Bragg's Law ($\lambda = 2\,n\,d\,\sin\theta$; λ is the diffraction wavelength, n is the refractive index of water, d is the lattice plane spacing, and $\theta = 90°$ is the Bragg normal incidence angle)[22]. It decreases from 263 to 220 nm as the strength of electromagnetic field increases (Figure 3c) from 9.5 to 22.2 mT. Note that the inter-particle distance actually

affects the electromagnetic (EM) field distribution in the vicinity of a metal surface, which further influences the SERS signal of target molecules[23]. This is why the knowledge of the inter-particle distance of a quasi-photonic crystal is important for practical SERS detection, which will be discussed in the next section. Also note that the reflection spectra of the Fe_3O_4/Au NPs system did not change by adsorption of probe or analyte molecules, *e.g.* Rhodamine 6G (R6G). This is due to the small volume ratio and low concentration of the added organic dye molecules, which are insufficient to change the effective refractive index inside the quasi-photonic crystal system.

SERS of Fe_3O_4/Au NPs quasi-photonic crystal system. In the previous sections the structure of the Fe_3O_4/capped Au NPs was determined and proven to exhibit quasi-photonic crystal properties, which are tunable by an external magnetic field. The next section evaluates the SERS efficacy of the quasi-photonic system. The Raman experiments were conducted employing R6G as the model molecule due to its well-established vibrational features[24,25]. The Raman signal of Au/Fe_3O_4 colloidal solution is very low and has negligible influence on probe molecules for SERS experiment. 20 μL of 1×10^{-6} M R6G solution was dropped into 180 μL (about 6 mg) as-prepared Fe_3O_4/Au NPs dispersion. The mixture was transferred in a quartz cuvette (~350 μL in volume) with a quartz window, which was then placed onto an electromagnet, the intensity of which can be modulated from 0 to 39.6 mT.

The Raman spectrum of a 0.01 M R6G was measured first serving as a reference spectrum (Figure 4a) for the following SERS EF measurements. Next, the Raman spectra (Figures 4b and 4c) of a $1 \times$
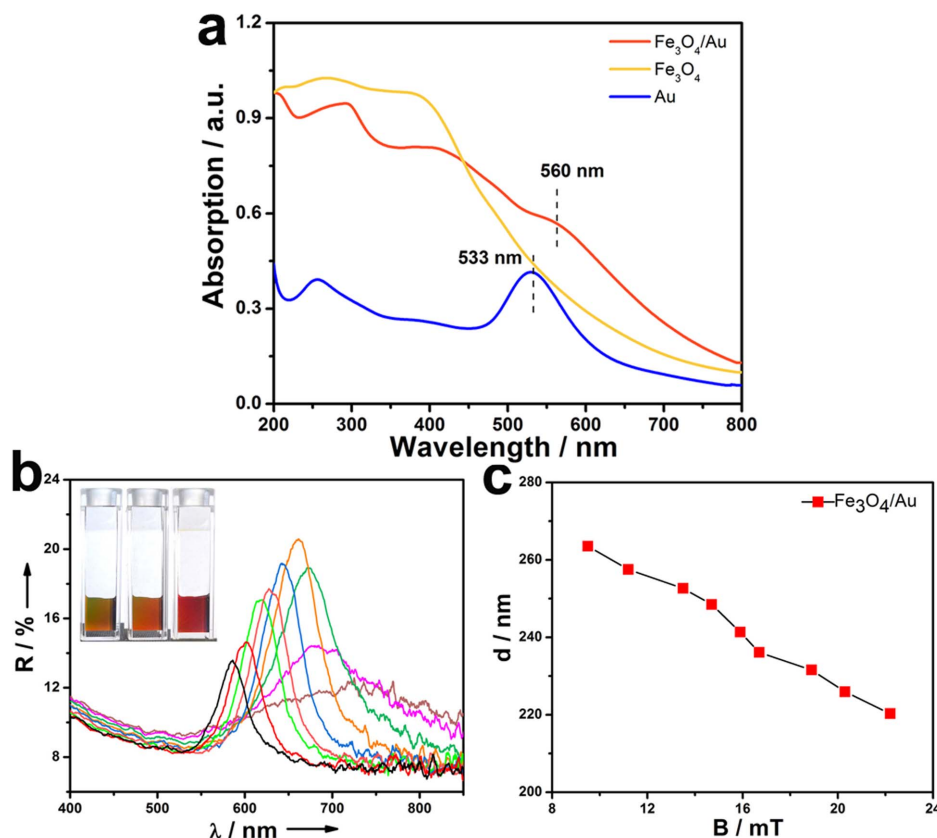

Figure 3 | (a) UV-vis spectra of the Fe_3O_4/Au NPs (red) (volume ratio of Au : Fe_3O_4 = 40 : 1), pure Fe_3O_4 nano-colloidal solution (yellow), Au NPs (blue). All particles were dispersed in water and the concentrations were 0.22 mg·mL^{-1}, 0.26 mg·mL^{-1} and 0.12 mg·mL^{-1}, respectively; (b) Reflection spectra of Fe_3O_4/Au quasi-photonic system (volume ratio of Au : Fe_3O_4 = 40 : 1) in response to an external magnetic field. Diffraction peaks blue-shift (from right to left) as the magnetic field increases from 9.5 to 22.2 mT by increasing the electric current from 0.035 to 0.075 A. The inset shows that the color changed as the magnetic field increased; and (c) The inter-particle distance was calculated to vary between 263 nm to 190 nm as the magnetic field increases from 9.5 to 22.2 mT.
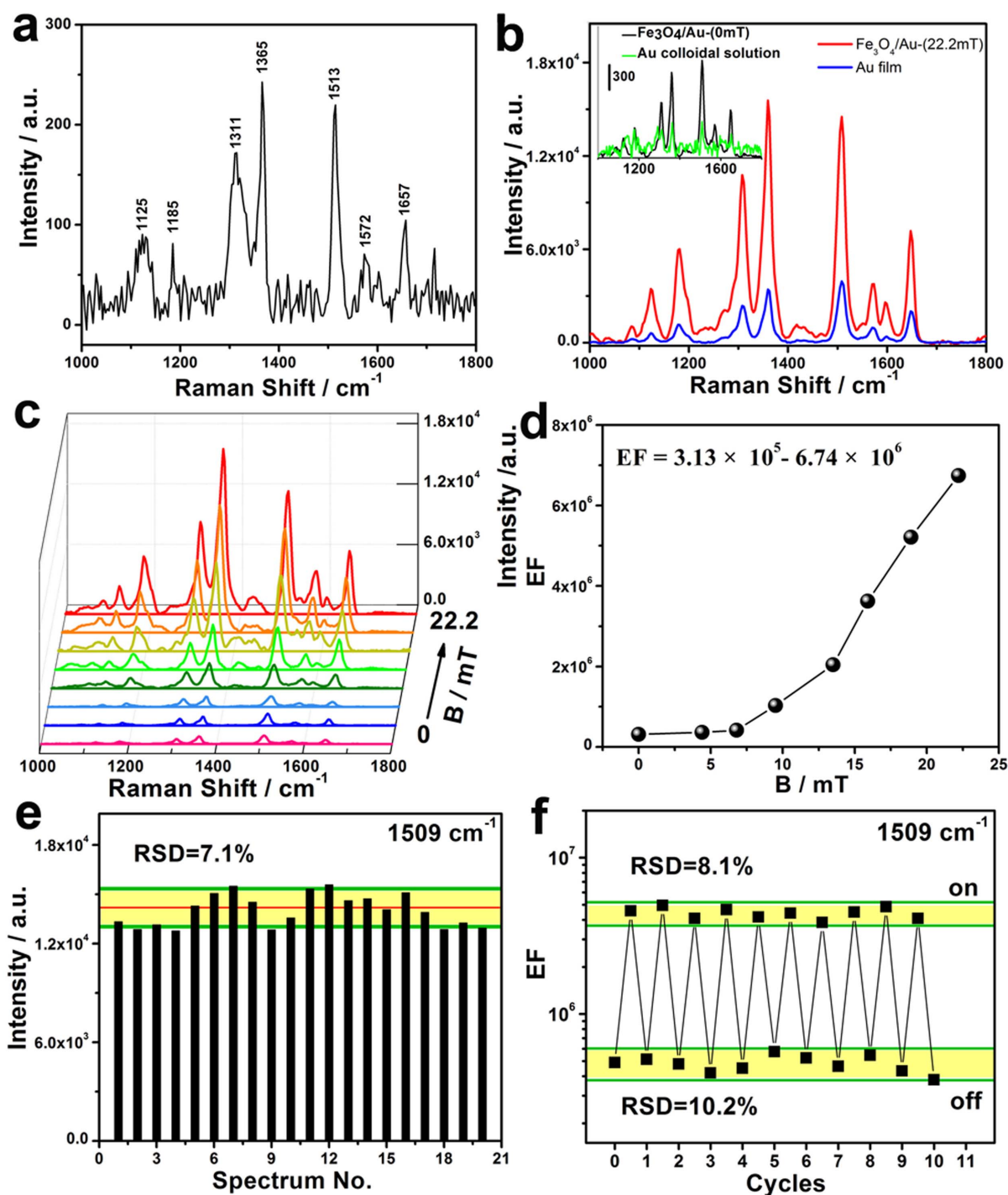
Figure 4 | (a) The Raman reference spectrum of the 0.01 M R6G solution; (b) SERS of R6G solution (1×10^{-7} M) enhanced by an Au film (Au NPs spin-coated onto silicon wafer as in Figure 1c), by pure Au colloidal solution and by the Fe_3O_4/Au periodic system (0 mT and 22.2 mT); (c) The evolution of the SERS of R6G solution (1×10^{-7} M) on Fe_3O_4/Au NPs quasi-photonic system (volume ratio of Au : $Fe_3O_4 = 40 : 1$) with the increasing external magnetic field; (d) The calculated EF derived from the R6G 1509 cm^{-1} lines of spectra 4(c) with the increasing external magnetic field; (e) The intensity variation of the 1509 cm^{-1} R6G peak at 20 different spots. The spot-to-spot RSD = 7.1%; and (f) The SERS intensity of the 1509 cm^{-1} R6G peak in response to 10 on-off external magnetic field cycles of 18.9 mT indicates reversible SERS detection with RSD = 8.1% for the on peak and 10.2% for the off peak.

10^{-7} M R6G solution was measured on three different substrates: (1) an Au film dispersed on a silicon wafer by spin coating of the Au NPs (the morphology of which was previously shown in Figure 1c); (2) a liquid Fe_3O_4/Au substrate exposed to a varying magnetic field in the range of 0–22.2 mT; (3) a pure Au colloidal solution. The spectra of first two samples show the intense peaks of R6G's main vibrational features of carbon skeleton stretching modes at 1311, 1360, 1509,

1573, and 1650 cm^{-1}, which are similar to those of the reference 0.01 M Raman spectrum. However, the distance between Au nanoparticles in colloidal solution is much uncontrollable and larger than that in the first two substrates, which leads to low SERS intensity and reproducibility. Note that increasing the external magnetic field from 0 to 22.2 mT increased the SERS intensity of R6G in the Fe_3O_4/Au quasi-photonic system. The SERS intensity of the Au film was larger
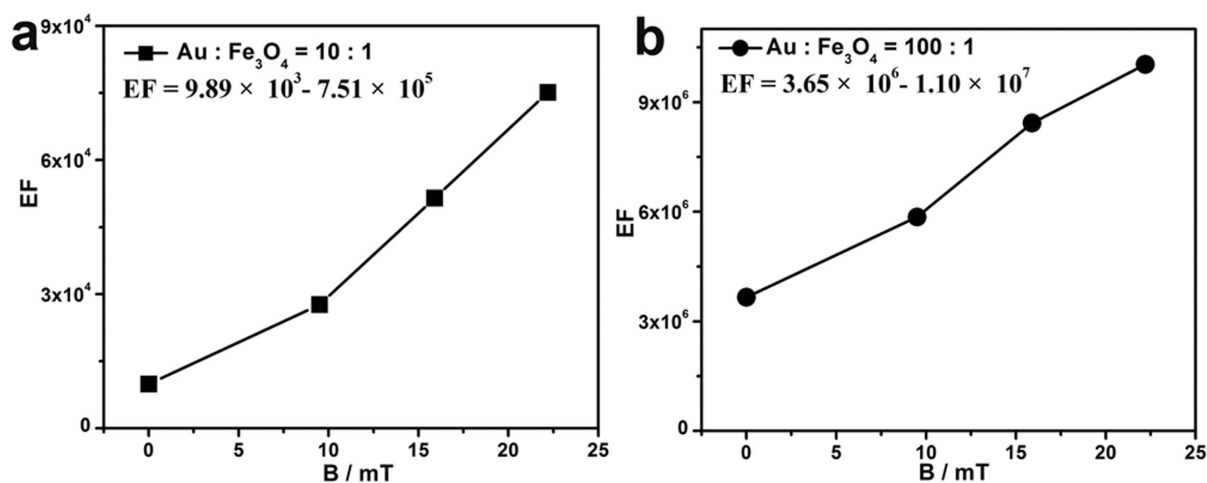
Figure 5 | Calculated EF values (derived from the 1509 cm^{-1} Raman peak) with increasing external magnetic field: (a) R6G solution (1×10^{-5} M) using the Fe$_3$O$_4$/Au NPs system (volume ratio of Au : Fe$_3$O$_4$ = 10 : 1), and (b) R6G solution (1×10^{-7} M) using the Fe$_3$O$_4$/Au NPs system (volume ratio of Au : Fe$_3$O$_4$ = 100 : 1).

than that of the liquid Fe$_3$O$_4$/Au substrate under zero magnetic field, but was much smaller than that of the same substrate under 22.2 mT.

For quantification, the EF values of the different experiments were calculated using: $EF = \dfrac{I_{SERS}N_0}{I_0 N_{SERS}}$, where I$_0$ and I$_{SERS}$ are the peak intensity of the Raman measurement with the reference (here 0.01 M) R6G solution and the peak intensity of the SERS, respectively; N$_0$ and N$_{SERS}$ are the number of R6G molecules in the scattering volume for the Raman measurement and SERS measurement, respectively. Since the experiments were conducted in a solution, the EF equation may be re-written as[26]: $EF = \dfrac{I_{SERS}C_0}{I_0 C_{SERS}}$, where C_0 and C_{SERS} are the concentrations of the reference R6G sample and the SERS R6G sample.

The calculated EF values (based on the intensity of the carbon skeleton stretching modes at 1509 cm^{-1}) are shown in Figure 4d. The EF values increase from 3.13×10^5 to 6.74×10^6 when increasing the external magnetic field from 0 to 22.2 mT. The spot-to-spot reproducibility (an important requirement for quantitative SERS measurements) of the liquid Fe$_3$O$_4$/Au NPs substrate was checked by conducting SERS measurements at 20 randomly chosen spots applying a magnetic field of 22.2 mT. The intensity variation for the 1509 cm^{-1} peak had a standard deviation of 7.1% (Figure 4e). The reversibility of the magnetic tuning of the system was studied as well in Figure 4f by measuring the EF (of the 1509 cm^{-1} Raman mode) in 10 consecutive on-off magnetic field cycles (off - 0 mT, on - 18.9 mT). The standard deviation of the on EF was 8.1% while that of the off EF was 10.2%. In addition, the EF of the pure Au suspension (with R6G = 10^{-7} M) was 1.31×10^5 compared to 3.13×10^5 for the Fe$_3$O$_4$/Au system with 0 magnetic field and 1.62×10^6 for the solid Au target and does not depend on the magnetic field. The Au suspension shows low reproducibility for quantitative detection and less order than that achieved in a liquid solution by attachment to the Fe$_3$O$_4$ particles which are round and have a small size distribution in a liquid solution. It is also inferior to a solid Au target made by spin coating.

Finally, we checked the adjustability of the system to different analyte concentrations. As the requested concentration measurement level of the analyte increases, the EF should be reduced. This is very readily accomplished in the present Fe$_3$O$_4$/Au system by reducing the relative amount of Au NPS with respect to the Fe$_3$O$_4$ NPs (reducing the EF). A volume ratio of 10 : 1 CTAB-capped Au suspension to as-prepared Fe$_3$O$_4$ suspension is needed for a R6G concentration level of 10^{-5} M (Figure 5a), while a much larger

volume ratio of 100 : 1 is needed for SERS detection of R6G with a concentration level of 10^{-7} M (Figure 5b). Note that the tunable range of the EF by an external magnetic field varying from 0 to 22 mT is medium (9.89×10^3–7.51×10^4) for a volume ratio of 10 : 1. It increases to 3.13×10^5–6.74×10^6 for a volume ratio of 40 : 1 (Figure 4d). It decreases to 3.65×10^6–1.10×10^7 when the Au: Fe$_3$O$_4$ volume ratio increases to 100 : 1. The choice of the appropriate Fe$_3$O$_4$/Au SERS system should thus be made as a tradeoff between the demand of high SERS activity (high EF) and the request of a large tunability of EF by an external magnetic field.

Application - Use of the Fe$_3$O$_4$/Au tunable liquid SERS substrate in a quantitative detection. The tunability of the Fe$_3$O$_4$/Au liquid SERS substrate is usable for precise analyte measurements with an internal calibration standard. For that purpose the internal standard is introduced at a specific fixed concentration along with different concentrations of the analyte to be tested. A calibration curve of the analyte signal intensity versus the analyte concentration is then measured fixing the EF of the standard to a pre-determined value by tuning the external magnetic field to reach this EF value. In the present work R6G was employed as the internal standard and crystal violet (CV) as the analyte. Figure 6a shows the SERS of R6G (1×10^{-7} M), CV (1×10^{-7} M) and the mixture of both for the Fe$_3$O$_4$/Au system (Au : Fe$_3$O$_4$ volume ratio 40 : 1) at B = 0. Obviously the 1509 and 1618 cm^{-1} Raman modes of R6G and CV respectively do not overlap with other modes, enabling their use for setting up a calibration curve with an internal standard. The Fe$_3$O$_4$/Au substrates with a fixed concentration of R6G of 1×10^{-7} M and varying concentrations of CV in the range of 1×10^{-8}–1×10^{-6} M were then prepared. The external magnetic field was applied to tune the EF value (measured using the R6G 1509 cm^{-1}) to 2×10^6. The fixation of R6G's EF aims to minimize experimental variations (e.g., substrate-to-substrate differences). Figure 6d shows the calibration curve of I_{CV} (1618 cm^{-1} peak intensity of CV) versus C_{CV} (concentration of CV) at EF = 2×10^6: $\log(C_{CV}) = -10960 + 1.103 \log(I_{CV})$ with a correlation coefficient of R = 0.995. Determination of an unknown quantity of CV can be performed by mixing it with a Fe$_3$O$_4$/Au liquid target with 1×10^{-7} M, setting EF to 2×10^6 and using the calibration curve. Figure 6e shows the EFs of R6G (using the 1509 cm^{-1} Raman line) with different concentrations of CV ranging from 10^{-8} to 10^{-6} M. Note that the variations of the EF with different concentrations of CV are less than 8%. Moreover, the relative standard deviation (RSD) of the EF values in these measurements reflect the total variations of the
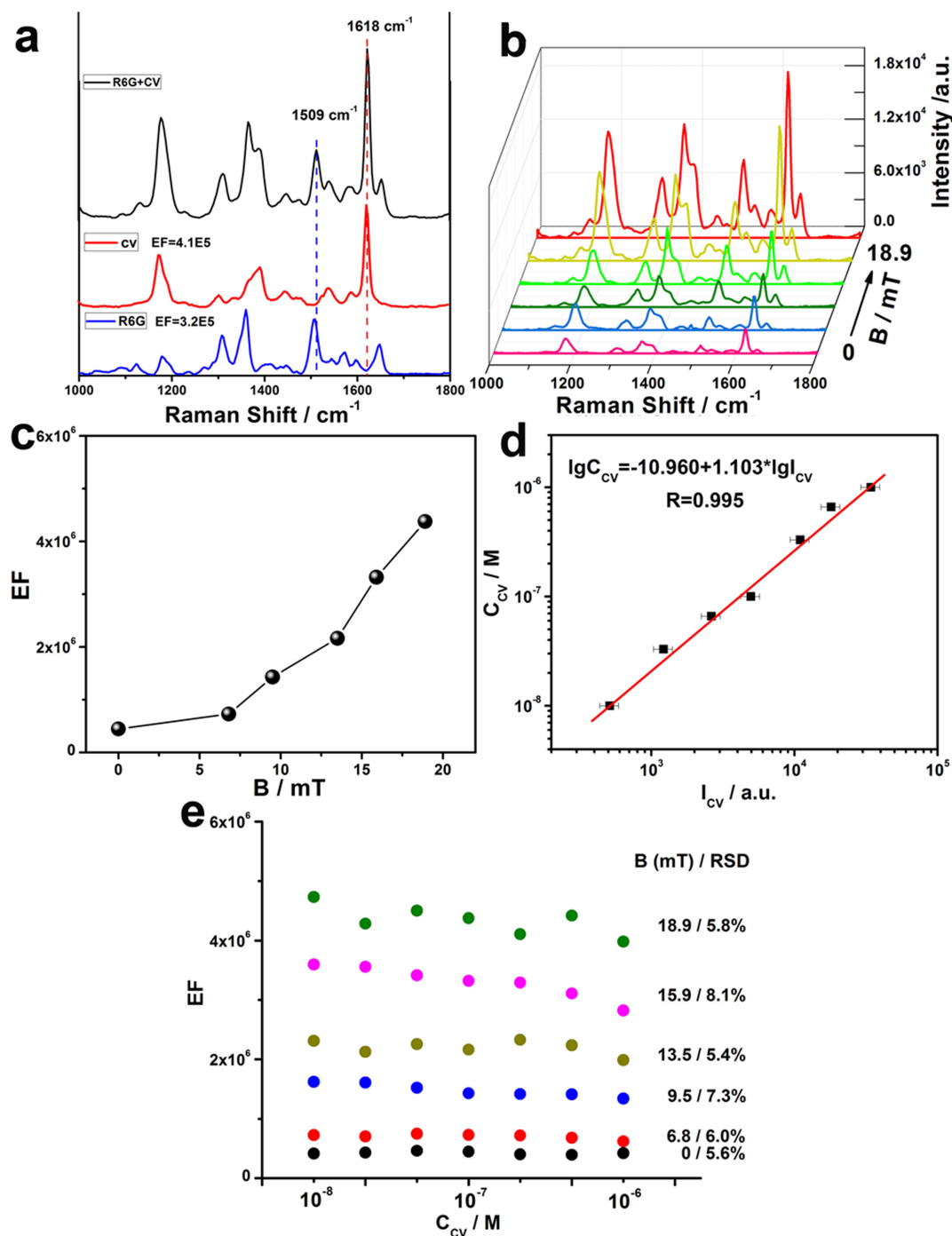
Figure 6 | (a) SERS of R6G (1×10^{-7} M), CV (1×10^{-7} M), and the mixture of R6G and CV (both are 1×10^{-7} M) using the Fe_3O_4/Au NPs system (volume ratio of Au : Fe_3O_4 = 40 : 1) under magnetic field intensity of zero; (b) SERS of the mixture of R6G and CV (both are 1×10^{-7} M) using the Fe_3O_4/Au NPs system (volume ratio of Au : Fe_3O_4 = 40 : 1) with the external magnetic field intensity ranging from 0 to 18.9 mT; (c) The calculated EF from the 1509 cm^{-1} Raman R6G lines of Figure 6 (b) with the increasing magnetic field; and (d) The calibration curve of the concentration of CV (10^{-8}–10^{-6}M) vs. the CV SERS intensity (1618 cm^{-1}) based on Fe_3O_4/Au NP system (volume ratio of Au : Fe_3O_4 = 40 : 1) under the EF value of 2×10^6 for R6G (1509 cm^{-1}) for quantitative detection; (e) EF values of R6G (derived from the 1509 cm^{-1} Raman peak) of a 10^{-7}M R6G solution mixed with different concentrations of CV (10^{-8}–10^{-6}M). The RSD of the measurements for different B values is indicated in the figure. Note the low values of RSD which reflect the high homogeneity and reproducibility of the Fe_3O_4/Au system even for mixtures of analytes.

system including spot-to-spot inhomogeneity and instability of the magnetic field for different measurements. These results thus indicate that a high level of accuracy is indeed achievable when using the Fe_3O_4/Au system.

Simulation of tunable EF with Fe_3O_4/Au NPs quasi-photonic crystal system. The penetration of the electromagnetic field to a

quasi-photonic crystal with different inter-particle distances ranging from 220 to 260 nm (as found experimentally, see Figure 3c) was calculated using a 3D-finite difference time domain (FDTD) software as fully described in the Methods section. The Fe_3O_4 particles were ordered as described in Figure 7. The Au particles bonded to the Fe_3O_4 particles were simulated by a 1 nm thick film surrounding the surface of the Fe_3O_4 particles. The
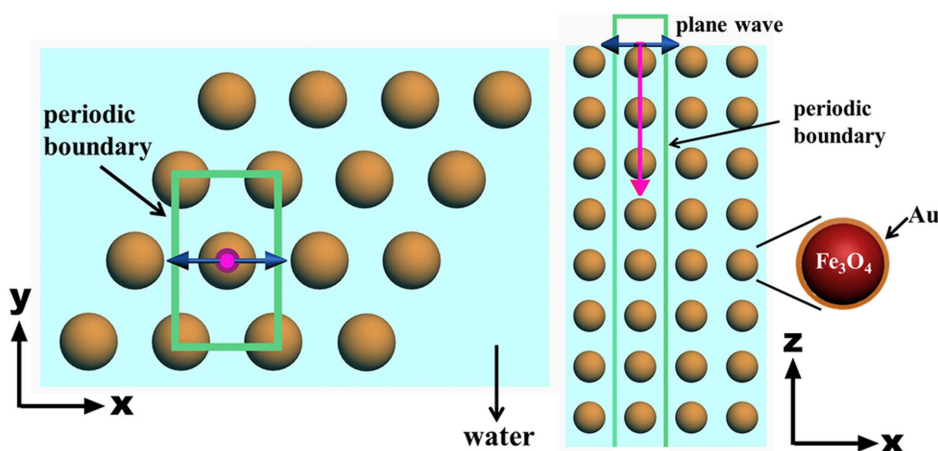
Figure 7 | Schematic representation of the Fe₃O₄/Au NPs quasi-photonic crystal system in the FDTD simulation in the x-y plane (left) and the x-z (right). The incident light is a plane wave which propagated along the z direction with polarization in the x direction.

electromagnetic wave propagates from top to bottom in the *x-z* plane with planar polarization in the x direction (Figure 7 right) and perpendicular to the *x-y* plane as indicated in Figure 7 left. This model cannot accurately predict the characteristics of real Fe₃O₄/Au NPs nanostructures because of the calculation complexity caused by the inhomogeneous and random distribution of large spheres (Fe₃O₄ NPs) and small ones (Au NPs). The simulations however demonstrate (Figure 8) the effect of the inter-particle distance on the penetration of the electric-field to the photonic crystal. The decrease of the inter-particle distance from 260 to 220 nm increased the penetration of the electromagnetic field to the Fe₃O₄/Au quasi-photonic system and clearly formed large electromagnetic fields (hot spots) around the Au film. As we know, SERS signals linearly increase with the squared product of the local field enhancements at the excitation and Raman scattering wavelengths[23]. The distance between Au nanoparticles in solution substantially affects the field intensity induced by localized surface plasmon resonance (LSPR). The interwind correlation between the plasmon resonance and the Raman scattering wavelength might yield different EFs for different Raman peaks that may change with respect to each other as the magnetic field is varied (modifying the interparticle distance and the plasmon resonance). These results are in accord with the enhancement of the Raman signal by provision of an external magnetic field which reduces the inter-particle distance.

Discussion

Regular SERS substrates are solid substrates, which adsorb the analyte to be monitored. Their EF is achieved by a variety of patterning techniques and cannot be readily predicted nor can it be tuned to reach specific pre-determined values. Consequently solid SERS substrates are characterized by a limited spot-to-spot homogeneity, insufficient reproducibility, and questionable stability. Precise control of the EFs of these solid substrates is still a challenge.

Liquid tunable photonic crystals based on a suspension of Fe₃O₄ NPs were recently reported for a variety of possible applications[18–20]. Tuning by an external magnetic field provides excellent control of the inter-particle distance in Fe₃O₄ NPs suspension and thus manipulation of their optical properties. However, utilization of a liquid Fe₃O₄ system for SERS has not been reported by now, to the best of our knowledge. In the present work we harnessed together surface Raman-active Au NPs with Fe₃O₄ NPs by initiation of attractive electrostatic forces within the processing method (fabrication of negatively charged Fe₃O₄ NPs and positively charged CTAB capped Au NPs). The fabrication process provides uniform-sized Fe₃O₄ particles of 180 nm in diameter (Figure 1a). Our newly developed system was found to be able to blue-shift the reflection peak by

introduction of an external magnetic field (Figure 3b). The inter-particle distance of the photonic crystal formed was determined by the equilibrium between the external magnetic force and the internal electrostatic forces. The coupling between the SERS-active Au NPs producing surface plasmons and the electromagnetic field induced by the photonic crystal generated by the Fe₃O₄ NPs not only initiated high EF values of 10^4 to 10^7, but also enabled the tunability of the EF values obtained by an external magnetic field (Figures 4 and 5). The combined effect of the quazi-photonic crystal and the Au particles on the electromagnetic field penetration was also verified by simulations (Figure 8). The EF values covering the range of 10^4-10^7 are readily adjustable by the volume ratio between the Fe₃O₄ NPs and the Au NPs (Figure 5). Once the $B = 0$ EF value is determined, the EF can be further tuned by varying the external magnetic field within a range which depends on the $B = 0$ EF (Figure 5). It is interesting to note that the EF obtained by an Au film dispersed on a solid substrate (blue curve in Figure 4b) is larger than that obtained by the Fe₃O₄/Au system at $B = 0$ (black curve in Figure 4b). This is due to the better order achieved in dispersing the Au NPs as a solid film compared to a Fe₃O₄/Au suspension. Introduction of an external magnetic field however compresses the 3D crystal of the Fe₃O₄ NPs and introduces a much better order resulting in significantly higher EF values (red curve in Figure 4b). The ordering effect is similar to that obtained by pressing amphiphilic molecules forming self assembled monolayers (SAM) in Langmuir Blogdet films.

The novel liquid SERS substrate based on the Fe₃O₄/Au system (Figure 9, the detailed description of the system is listed in the Method section) possesses a host of advantages for quantitative SERS analysis. It offers a simple way of controlling the EF values: (1) a coarse adjustment of EF by the choice of the relative concentrations of the Fe₃O₄ and Au NPs followed by (2) a final precise tuning to a preset value by the external magnetic field. The combined use of a liquid solution and the ordering imposed by the external magnetic field leads to good spot-to-spot homogeneity and reproducibility (Figure 4). The liquid substrate further offers a simple introduction of the analyte to be tested. The reversible tuning by the external magnetic field enables the use of internal standards and obtaining calibration curves with an estimated accuracy equal or better than 10% (see the example given in a previous section and Figure 6). We thus believe that this host of advantages offered by the Fe₃O₄/Au NPs-based liquid SERS substrate presents a significant step forward in establishing SERS as a quantitative technique.

This work introduces the Fe₃O₄/Au NPs suspension as a smart tunable liquid SERS substrate. The attachment of the NPs to the Fe₃O₄ particles to produce this system was achieved by electrostatic attraction. The suspension was first shown to assemble a quasi-peri-
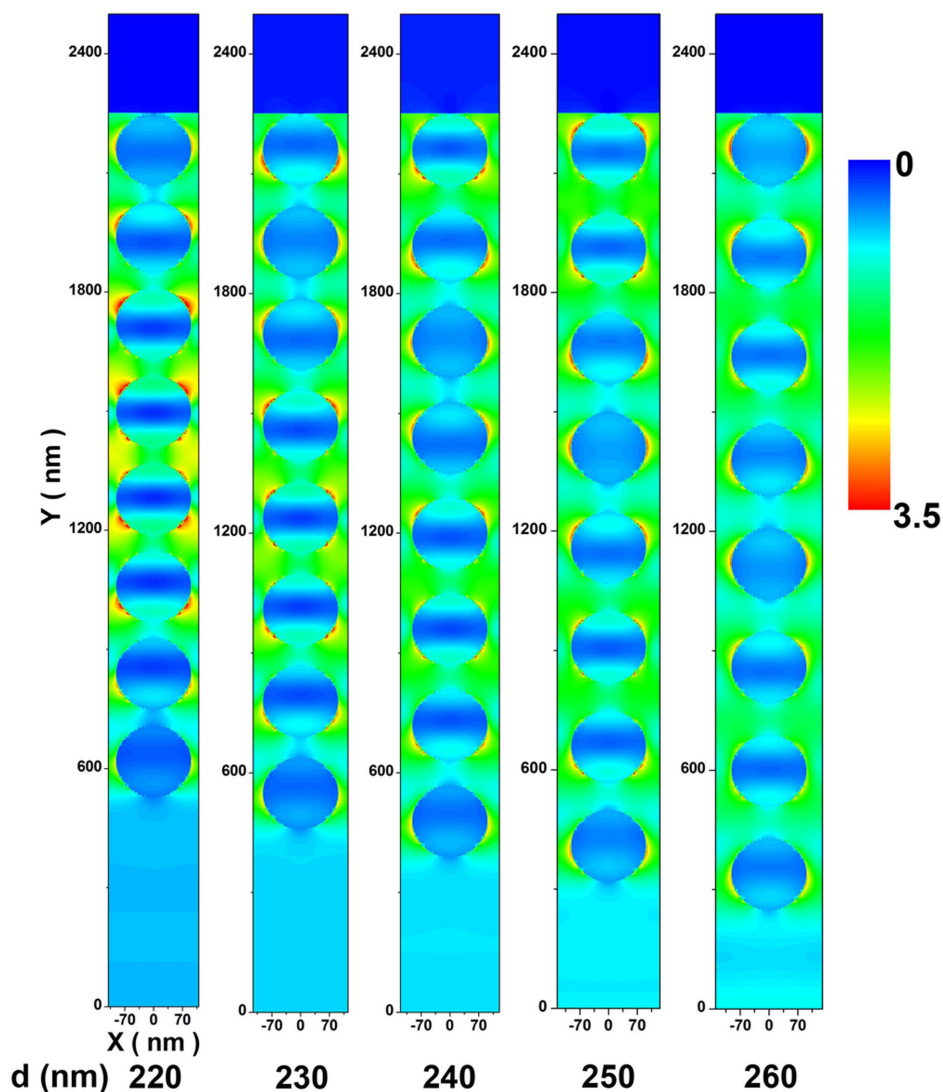
Figure 8 | The simulated electromagnetic field distribution in the x-z plane of the Fe_3O_4/Au NPs quasi-photonic system with different inter-particle distance from 220 to 260 nm (left to right).

odic crystal by application of an external magnetic field, which reduces the inter-particle distance in a reversible manner, forces order and modifies the optical properties (e.g. blue-shifts the reflection spectra). The Fe_3O_4/Au NPs system couples localized surface plasmon resonance with the photonic crystal formed initiating surface enhanced Raman activity in a tunable and reversible way. The EFs can be consequently tailored in the range of 10^4–10^7 by changing the relative volumes of Au: Fe_3O_4. Additionally the EFs can be reversibly tuned by an external magnetic field in the range of one to two orders of magnitude depending on the Fe_3O_4/Au composition. The system is characteristic of high spot-to-spot reproducibility and high reversibility. The ability to reversibly adjust the EF values minimizes the influence of external factors which may cause variability of the SERS activity (such as substrate-to-substrate differences and long-term-storage degradation). The above listed properties of the novel Fe_3O_4/Au based liquid SERS substrate may significantly contribute to more accurate quantitative applications of SERS.

Methods

Materials. Ammonium ferric citrate ($FeC_6H_5O_7 \cdot NH_4OH$), polyacrylic acid (PAA, molecular weight = 3000), hydrazine hydrate ($N_2H_4 \cdot H_2O$, 85%), and sodium borohydride ($NaBH_4$) were all purchased from Alfa Aesar Co. Cetyltrimethylammonium bromide (CTAB) and hydrogen tetra-chloroaurate(III) tetrahydrate ($HAuCl_4 \cdot 4H_2O$) were purchased from Sinopharm Group Chemical regent Co., Ltd. (Shanghai, China). Other reagents were of analytical reagent grade and used without further purification. Ultrapure water was used in the experiment.

Synthesis of Fe_3O_4 NPs. Fe_3O_4 superparamagnetic colloidal NPs were synthesized by using a high-temperature hydrolysis reaction. In the preparation of Fe_3O_4 NPs, poly
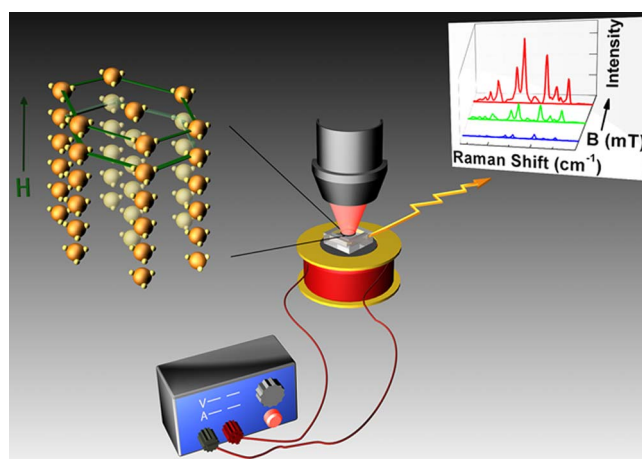
Figure 9 | The schematic of the setup in the SERS detection with reversibly tunable EF based on smart liquid substrates.

acrylic acid (PAA) was chosen for the process because of the strong coordination of carboxylate groups with iron cations on the magnetite surface, which confers on the particles a uniform size and a high degree of dispersibility in water. In a typical procedure, 0.30 g $FeC_6H_5O_7 \cdot NH_4OH$ was dissolved in 12 mL water to form a clear solution. Under stirring of an electric mixer, 4 mL PAA was added dropwise. After 1 h, 4 mL $N_2H_4 \cdot H_2O$ (85%) was added. The final mixture was stirred for another 30 min and subsequently transferred into a 30 mL Teflon-lined stainless-steel autoclave. The autoclave was maintained at 180°C for 10 h. The black product (about 70 mg) was collected after it was cooled to room temperature, washed with ultrapure water for several times, and then dispersed in 2 mL of ultrapure water.

Preparation of CTAB-capped Au NPs. CTAB-capped Au NPs were prepared by reduction of chloroauric acid solution in a one-step procedure. First, 8.0 mL CTAB (1.0×10^{-3} M) was added gradually to 40 mL $HAuCl_4 \cdot 4H_2O$ (2.5×10^{-4} M) in the presence of magnetic stirring, and then 1.8 mL freshly prepared ice-cold $NaBH_4$ (6.0×10^{-3} M) were added at once to the solution. After being mixed vigorously for about 20 min, the mixed solution was left undisturbed for 24 h at 25°C.

Preparation of Fe3O4/Au NPs. The Fe_3O_4/Au NPs can be obtained by a simple method of electrostatic attraction. In a typical procedure, 2 mL as-prepared Fe_3O_4 (about 70 mg) superparamagnetic colloidal NPs were added slowly in 80 mL as-prepared CTAB-capped Au NPs under vigorous stirring (To achieve a volume ratio of Au : Fe_3O_4 = 40 : 1. Volume ratios of 10 : 1 and 100 : 1 were also applied). After 2 h electrostatic adsorption, the prepared Fe_3O_4/Au NPs should be collected and cleaned with ultrapure water three times to eliminate the gold NPs weakly absorbed. Then Fe_3O_4/Au NPs (about 60 mg) were dispersed in 2 mL ultrapure water.

Characterization. The phase and the crystalline structure of the products were characterized by X-ray powder diffraction (XRD, a Philips X' pert PRO MPD diffractometer) with Cu Kα radiation (λ = 0.15406 nm). The size and morphology of samples were monitored using a Zeiss Supra 55 field scanning electron microscope (SEM) operating in high vacuum mode with an acceleration voltage of 15 kV. TEM, HRTEM, STEM and elemental mapping by EDS analysis were performed by a FEI Tecnai F20 transmission electron microscope with an accelerating voltage of 200 kV. The ultraviolet-visible (UV-vis) absorption spectrum was recorded by a Thermo Scientific Evolution 220 Diode Array Spectrophotometer. Raman spectra were measured with an HR 800 Raman spectrometer (J Y, France) equipped with a synapse CCD detector and a confocal Olympus microscope. The spectrograph was operated with 600 g/mm gratings and a 633 nm He-Ne laser was applied for excitation. SERS spectra were collected by an objective with a magnification of x50 (Olympus) with a numerical aperture of 0.90 and an accumulation time of 1 s. SERS experiments were conducted in the line mapping mode with 1 μm increments using 1×10^{-7} M R6G water solution.

Setup of the experiment. Figure 9 shows the schematic of setup in the SERS detection with reversibly controllable EFs. Fe_3O_4/Au dispersion, together with the analyte, was introduced to the quartz cuvette closed by a quartz window. The cuvette was placed onto an electromagnet, the magnetic field intensity of which can be modulated by the electric current. Both the cuvette and electromagnet were positioned under the Raman microscope. In the process of Raman detection, the laser was focused on the surface of Fe_3O_4/Au dispersion through the quartz window.

Theoretical calculations. In order to model theoretically the plasmon coupling in the Fe_3O_4/Au system, 3D-FDTD simulations were performed with FDTD Solutions from Lumerical Solutions, Inc. (Vancouver, Canada). A frequency-domain field profile monitor was used to record the electromagnetic field over the simulation region. Figure 7 clearly shows the FDTD simulation conditions. The simulated photonic crystal was constructed of Fe_3O_4/Au spheres array with hexagonal arrangement in the x-y plane (Figure 7 left) and reduplicative arrangement of 8 layers of Fe_3O_4/Au in the x-z plane. The diameter of Fe_3O_4 spheres was 180 nm and the thickness of Au film was 1 nm, respectively. This Au film was employed to represent the Au NPs in the real Fe_3O_4/Au system. Periodic boundary conditions were applied to the x- and y-directions to describe an infinite array, and perfectly matched layers (PML) were set to the z-boundaries as a boundary condition. The spheres were surrounded by water, and a p-polarized 633 nm plane wave was placed above the water and polarized to the x-axis. The refractive index of Fe_3O_4 and water were set as 1.33 and 2.42, respectively. The experimental value of Palik[27] was used for the dielectric constant of Au. The mesh size used in the calculations was 1 nm $\times$ 1 nm $\times$ 1 nm. The simulation time was set at 500 fs, ensuring the fields to decay completely before termination of the simulation. The distance between each sphere d (260–220 nm) corresponded to the experimental results (Figure 3c). To obtain the electric field distribution around the Fe_3O_4/Au NPs, an x-z plane monitor was placed through the centre of sphere. The electric field intensity distribution was reported as the square of the electric field ($|E/E_0|^2$).

1. Freeman, R. G. et al. Self-assembled metal colloid monolayers - an approach to SERS substrates. *Science* **267**, 1629–1632 (1995).
2. Nie, S. M. & Emery, S. R. Probing single molecules and single nanoparticles by surface-enhanced Raman scattering. *Science* **275**, 1102–1106 (1997).
3. Li, J. F. et al. Shell-isolated nanoparticle-enhanced Raman spectroscopy. *Nautre* **464**, 392–395 (2010).
4. Kneipp, K. et al. Single molecule detection using surface-enhanced Raman scattering (SERS). *Phys. Rev. Lett.* **78**, 1667–1670 (1997).
5. Fleischmann, M., Hendra, P. J. & McQuillan, A. J. Raman spectra of pyridine adsorbed at a silver electrode. *Chem. Phys. Lett.* **26**, 163–166 (1974).
6. Liu, H. et al. Single molecule detection from a large-scale SERS-active $Au_{79}Ag_{21}$ substrate. *Sci. Rep.* **1**, 112; DOI:10.1038/srep00112 (2011).
7. Ma, W. et al. Investigating electron-transfer processes using a biomimetic hybrid bilayer membrane system. *Nature Protocol.* **8**, 439–450 (2013).
8. Chen, Z. et al. Protein microarrays with carbon nanotubes as multicolor Raman labels. *Nature Biotech.* **26**, 1285–1292 (2008).
9. Han, Y. et al. Towards Full-length accumulative surface-enhanced Raman scattering-active photonic crystal fibers. *Adv. Mater.* **22**, 2647–2651 (2010).
10. Natan, M. J. Surface enhanced Raman scattering. *Faraday Discuss.* **132**, 321–328 (2006).
11. Mulvihill, M. J., Ling, X. Y., Henzie, J. & Yang, P. D. Anisotropic etching of silver nanoparticles for plasmonic structures capable of single-particle SERS. *J. Am. Chem. Soc.* **132**, 268–274 (2010).
12. Diebold, E. D., Mack, N. H., Doom, S. K. & Mazur, E. Femtosecond laser-nanostructured substrates for surface-enhanced Raman scattering. *Langmuir* **25**, 1790–1794 (2009).
13. Wang, D. X., Zhu, W. Q., Chu, Y. Z. & Crozier, K. B. High directivity optical antenna substrates for surface enhanced Raman scattering. *Adv. Mater.* **24**, 4376–4380 (2012).
14. Im, H. et al. Self-assembled plasmonic nanoring cavity arrays for SERS and LSPR biosensing. *Adv. Mater.* **25**, 2678–2685 (2013).
15. Yang, L. L. et al. Engineering nanoparticle cluster arrays for bacterial biosensing: the role of the building block in multiscale SERS substrates. *Adv. Funct. Mater.* **20**, 2619–2628 (2010).
16. Zhao, Y., Zhang, X. J., Ye, J. & Lee, S. T. Metallo-dielectric photonic crystals for surface-enhanced Raman scattering. *ACS Nano* **5**, 3027–3033 (2011).
17. Tuyen, L. D., Liu, A. C., Huang, C. C. & Hsu, C. C. Doubly resonant surface-enhanced Raman scattering on gold nanorod decorated inverse opal photonic crystals. *Optics Express* **20**, 29266–29275 (2012).
18. Ge, J. P., Goebl, J., He, L., Lu, Z. D. & Yin, Y. D. Rewritable photonic paper with hygroscopic salt solution as ink. *Adv. Mater.* **21**, 4259–4264 (2009).
19. Kim, H. et al. Structural colour printing using a magnetically tunable and lithographically fixable photonic crystal. *Nature Photonics* **3**, 534–540 (2009).
20. Ge, J. P., Hu, Y. X. & Yin, Y. D. Highly Tunable superparamagnetic colloidal photonic crystals. *Angew. Chem. Int. Ed.* **46**, 7428–7431 (2007).
21. Yu, H. et al. Dumbbell-like bifunctional Au-Fe3O4 nanoparticles. *Nano Lett.* **5**, 379–382 (2005).
22. Xu, X. L., Friedman, G., Humfeld, K. D., Majetich, S. A. & Asher, S. A. Synthesis and utilization of monodisperse superparamagnetic colloidal particles for magnetically controllable photonic crystals. *Chem. Mater.* **14**, 1249–1256 (2002).
23. Kang, M. H., Kim, J. J., Oh, Y. J., Park, S. G. & Jeong, K. H. A deformable nanoplasmonic membrane reveals universal correlations between plasmon resonance and surface enhanced Raman scattering. *Adv. Mater.* **26**, 4510–4514 (2014).
24. Que, R. H. et al. Highly reproducible surface-enhanced Raman scattering on a capillarity-assisted gold nanoparticle assembly. *Adv. Funct. Mater.* **21**, 3337–3343 (2011).
25. Dieringer, J. A. et al. Surface-enhanced Raman excitation spectroscopy of a single Rhodamine 6G molecule. *J. Am. Chem. Soc.* **131**, 849–854 (2009).
26. Kim, K. et al. Interfacial liquid-state surface-enhanced Raman spectroscopy. *Nature Commun.* **4**, 2182 (2013).
27. Pailk, E. D. *Handbook of Optical Constants of Solids III.* (Academic Press, San Diego, 1998).

Acknowledgments

Author contributions

F.H. and H.L. contributed equally to the conception, planning of the project, performance of the experiments, and co-wrote the manuscript. M.S. and S.L. provided overall guidance in experimental design, experimental planning, data analysis and interpretation, scientific discussions throughout the project and manuscript writing. F.L. and Z.Z. performed the theoretical modelling and calculation. Y.L. participated in the data analysis, interpretation and manuscript writing.

Additional information